Crimson Publishers
Wings to the Research

Research Article

Green Synthesis of $NI_XCO_{X-1}O/COC_2O_4$ Nanocomposites from Fruit Juice, Characterization and Correlation of Dopant Concentration, Particle Size and Magnetic Properties

Ekane Peter Etape[1]*, Beckley Victorine namondo[1], Esther Dorcas Sama[1], Zoubir Benmaamar[2] and Josepha Foba Tendo[1]

[1]Department of Chemistry, Faculty of Science, University of Buea, Cameroon

[2]Department of Chemistry, Saad Dahlab University, Algeria

ISSN: 2578-0255

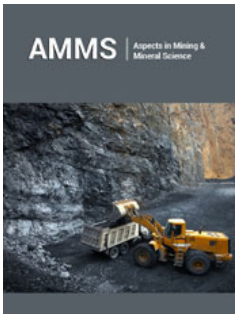

***Corresponding author:** Ekane Peter Etape, Department of Chemistry, Faculty of Science, University of Buea, Buea, Cameroon

Submission: May 12, 2023
Published: May 26, 2023

Volume 11 - Issue 3

How to cite this article: Ekane Peter Etape*, Beckley Victorine namondo, Esther Dorcas Sama, Zoubir Benmaamar and Josepha Foba Tendo. Green Synthesis of $NI_XCO_{X-1}O/COC_2O_4$ Nanocomposites from Fruit Juice, Characterization and Correlation of Dopant Concentration, Particle Size and Magnetic Properties. Aspects Min Miner Sci. 11(3). AMMS. 000764. 2023.
DOI: 10.31031/AMMS.2023.11.000764

Abstract

Magnetic nanoparticles with high surface area, size-dependent superparamagnetic behaviour such as precision, tunability, and easy surface modification have become good materials for biomedical applications. Based on the synthesis method, nanoparticles can be engineered and manipulated with other organic or inorganic functional compounds to form multimodal nanocomposites useful in the ragnosis. Accordingly, the nanocomposites of $Ni_xCo_{x-1}O/CoC_2O_4$ were fabricated by a single molecular metal organic (oxalate) precursor from carambola fruit juice and the corresponding metal chlorides. The solid metal oxalate precursors obtained from precipitation decomposed at 325 °C to the corresponding metal oxides/oxalate. The PXRD and EDS mapping images revealed $Ni_xCo_{1-x}O$ and CoC_2O_4. Nanoparticles coexisted in the composite while FTIR spectrum revealed the formation of cobalt oxalate metal organic framework without any surface adsorbed impurities. The Face cantered cubic phases of CoO with the particle size ranging from 9.0-15.0nm and CoC_2O_4 were assigned by the X-ray diffraction analysis. Nano tubes and cubic nano particle morphologies were identified from the Scanning Electron Microscopy (SEM) images and the variation in morphology and particle size was attributed to the presence of the nickel ion and the change in the concentration of the impurity ions. The magnetic properties exhibited by the synthesized Magnetic $Ni_xCo_{1-x}O/Co_3O_4$ Nanocomposites suggest that the as-synthesized nanocomposites have potential applications in negative contrast enhancing agents for Magnetic Resonance Imaging (MRI).

Keywords: Cobalt (II) oxide composite; Synthesis; Morphology; Particle size; Magnetism

Introduction

Despite the existing interdiction to clinical use that disincentives the exploitation and full potential use of cobalt oxide nanoparticles, there are various hints that cobalt based Nanoparticles (NPs) deserve to be further investigated to produce smart NPs usable in the ragnostic. Their magnetic properties, tunable, and regulated by external magnetic fields, can modulate multiple functions, such as imaging, photothermal, and pharmaceutical targeting of lesions, with minimally invasive procedures [1]. The use of nanoparticles such as cobalt oxide in technological applications has been based on other physical and chemical properties such as crystallinity, composition, morphology, and surface area [2]. The large surface-to-volume ratio and the shape of the nanoparticles are the main factors responsible for the novel highly exploited technological application properties. These physical, chemical, and mechanical properties are very different compared to those of the corresponding bulk material. Increasing the surface-to-volume ratio by reducing the particle size increases the fraction of the surface atoms with respect to the bulk ones [3].

Cobalt-based NPs, which behave as hard magnets, could be considered the possible counterpart of the soft magnets composed of iron oxide MNPs. The residual magnetization

is higher in MNPs with a core of cobalt oxide or cobalt–ferrite, in comparison with zero valent cobalt, while selected variants in the procedure for production, such as the temperature or the relative content of iron in cobalt–ferrite MNPs, can tune the saturation magnetization [4]. Magnetic nanoparticles have been synthesized using various methods: Co-precipitation [5]. Thermal decomposition [6], Hydrothermal [7], Chemical vapor condensation [8], Reverse microemulsion [9] Microwave [10] Electrochemical [11] but these methods have shown various drawbacks related to broader size distribution, toxic solvents, laborious procedures with large reaction time, high cost due to the use of specialized instruments, low yield and small scale production. The sizes and shapes of different types of nanoparticles are now being optimized using various methods of synthesis [12], such as combustion [13], aqueous combustion [14], Precipitation [15], (physical and chemical) methods while the literature shows that the method of synthesis has a direct effect on the microstructure of the nanoparticle.

Changes in microstructure have led to remarkable changes in physical properties such as particle size and shape. and morphology. Therefore, in the investigation of physical properties, it is crucial to pay attention to the method of synthesis and the structural features. A better, comprehensive, and satisfactory discussion of the magnetic properties of nanoparticles such as $Ni_xCo_{1-x}O$ cannot be done without some basic geometric features, namely: size, shape, composition, and crystal structure, and magnetic data such as temperature dependence magnetization, saturation magnetization, remnant magnetization and coercivity. The two main features that dominate the magnetic properties of nanoparticles and give them various special properties are: Finite-size effects (single-domain or multi-domain structure, and quantum confinement of electrons) and surface effect, which results from the symmetry breaking of the crystal structure at the surface of the particle (oxidation, dangling bonds, existence of surfactants, surface strain, or even different chemical and physical structures of internal "core" and surface "shell" parts of the nanoparticle) [15].

Cobalt exhibits various possible oxidation states but just (CoO and Co_3O_4) show stability in coordination including cubic, tetrahedral, pyramidal, and octahedral. Cobalt oxides offer an extensive spectrum of frameworks which are both stoichiometric and nonstoichiometric oxides, while involving a mixed valency of cobalt and/or the presence of oxygen vacancies. Cobalt oxide is specific to the 3d metal oxides, because cobalt oxide has the ability to manifest in three spin states: Low Spin (LS), High Spin (HS), and Intermediate Spin (IS). The occurrence of probable spin states brings a new insight into the physical chemistry of cobalt oxides in interest and complexity. The complexity in spin state is founded in the fact that the crystal field splitting dcf of the 3d energy level of the cobalt ion in cobalt oxides is of the same order of magnitude as the Hund's rule intraatomic exchange energy JH and the 3d-orbital bandwidth. In cobalt oxides, the selection suggested by the Hund's coupling ensures that Co^{2+} is always in high- spin state t_2g_5, eg_2 (S, ¼ 3/2) While for Co^{3+}, the three different spin states are possible (low-spin t_2g_6, eg 0 (S, ¼ 0), high-spin t_2g_4, eg_2 (S, ¼ 2), and intermediate spin t_2g_5, eg_1 (S , ¼ 1)) [16]. The dcf is very sensitive to changes in the Co-O bond length, and Co-O-Co bond angle which infer on the microstructure of the material.

Therefore, it is possible to modify with ease the spin state of Co^{n+} by varying the physical parameters such as pressure and temperature which will initiate Spin state transitions. This can be done by tuning the structural parameters such as oxygen content and type of counter cation of the material. The spin state of cobalt ions in its oxides is a function of the valence state, cation/anion ratio, and coordination number. These parameters have a frontline role in the engineering of technological applications (physical and structural) properties. The exciting peculiarity of cobalt oxides is the ability of the cobalt ions to express multiple functionalities in various valence states and different physical properties. When the Co^{2+} ion exhibits the high-spin state, the possibility of localizing an electron on the site forming a small polaron is easier and given the reduced transfer energy of the t_2g bands, it is difficult with an electron found on Co^{2+} to skip neither to the high-spin Co^{3+} nor to a Co^{3+} ion in the low-spin state since it is associated with a large spin flip from S ¼ 3/2 to S ¼ 0. This renders the pure Co^{2+} oxides magnetically insulating.

However, with the intermediate valence between Co^{2+} and Co^{3+} carriers are often confined to the Co^{2+} sites, which make the mixed Co^{2+}/Co^{3+} system to be sensitive to charge segregation and charge and/or spin ordering. As a consequence, the cobalt oxides having a cobalt valence state in +3 and +2 often exhibit high dielectric constants and magnetic behaviour. In the case of pure Co^{3+} oxides, the close competition between the crystal field splitting and the on-site exchange interaction often influences spin state transitions and/or crossover against physical stress such as temperature and pressure. Whereas Co_3O_4 has long been known and exhaustively documented, the chemistry and engineering of application properties of CoO is still meagre. CO_3O_4 is stable up to 800 ºC and decomposes to cobalt oxide CoO above 900 ºC. CoO nanocrystals display superparamagnetic or weak ferromagnetism, whereas bulk CoO is antiferromagnetic [17]. Soft Superparamagnetic nanoparticles such as iron- based, when exposed to an external variable magnetic field, rapidly and completely relax when the magnetic field returns to zero, whereas cobalt-based (CoB) hard magnets retain residual magnetization, a characteristic related with the procedure for Nanoparticles (NPs) production [1]. These properties are very interesting and while waiting for more experimental evidences documenting the in vivo toxicity of engineered CoB NPs which for now remain very few, we are still attracted by the potential of CoB NPs for theragnostic as multifaced signal probes for imaging, microrobots, enhanced thermo/radiation therapy, and drug release. $Ni_xCo_{x-1}O$ were modified with oxalate ions in the fabrication of a cobalt-based nanocomposite material expected to exhibit very interesting magnetic properties and to the best of our knowledge there is no literature existing for $Ni_xCo_{x-1}O/CoC_2O_4$ Composites. The study seeks to carry out a green synthesis of $Ni_xCo_{x-1}O/CoC_2O_4$ using carambola fruit juice and study

the morphological changes/magnetic effect of doping CoO/CoC_2O_4 with Nickel ions.

Materials and Methods

Materials

Co (II), Ni (II) chlorides ($CoCl_2.6H_2O$ and $NiCl_2.6H_2O$) were obtained from sigma Aldrich with 97% purity and were used without further purification. Fruit was extracted from fresh Carambola fruits.

Methods

Processing of fruit juice: Ripe carambola fruits were harvested from the campus of CRTV Buea in the South-West Region of Cameroon, washed under running tap water, and crushed in a domestic blender to produce a paste. The juice was extracted by squeezing the blended paste through a cheese cloth and centrifuged for 20min at 3000rpm [18,19]. The supernatant was collected and filtered. The filtration was kept in the freezer for further use.

Synthesis of the precursors: The Calculated doping fractions for Nickel used in the study are w/w%, x=0.0, 0.1, 0.3, 0.5, 1, 3, 5, 50 %. Solutions of various metal ions (Co^{2+} and Ni^{2+}) were prepared by dissolving the appropriate mass of the metal chloride in 100ml. of distilled water. 100ml of the juice extract were poured into a 250mL round bottom flask immersed into a water bath maintained at 80 °C. The appropriate metal ion solutions (200mL) are added slowly into the juice while stirring, and the mixture is stirred for a period of 2hrs. The mixture was allowed to cool to room temperature and the precipitates filtered, washed several times with distilled water, and dried in a glass oven at 100 °C for 1hr. The precursors obtained are identified and preserved for analysis and characterization.

Characterization of the samples: Thermal decomposition behaviour of the gels was studied using Netzsch (STA449C) DSC/TG. The patterns are collected as a function of temperature up to 900 °C under N_2 atmosphere. The heating rate of 10 °C/min. in N_2 is employed while alpha alumina is used as the reference material. The structural and functional groups of the samples were studied by Fourier Transform Infrared (FTIR) spectroscopy (Perkin Elmer, Model: spectrum one FT-IR spectrometer). FTIR analysis was carried out by using an FTIR Varian 600-IR, equipped with a Mercury Cadmium Telluride (MCT) detector and attached with ATR unit (PIKE MIRacle). Oven-dried powder samples are placed into the sample compartment of the ATR and pressed against the diamond crystal. Similar pressure is applied for all measurements by using the pressure applicator attached to a torque knob. The wavenumber range is chosen in the 4000-600cm^{-1} range with a 150 scan and resolution of 4cm^{-1}. The phase evolution of decomposed samples sintered at 350 °C for 3hrs was studied by powdered X-ray diffraction technique (Philips PAN analytical, Netherland) using CuKα radiation. The samples are scanned in the 2θ range 20 to 80 °C range in continuous scan mode with a scan rate of 0.02o/sec. Phases present in the sample are identified with the search match facility available in Philips X'pert high score software. The crystallite size of the calcined powders was determined from X-ray line broadening using the Scherrer's equation [16]:

$$t=0.9\lambda/B\cos\theta x$$

Where, t=crystallite size,

λ=wavelength of radiation,

θ=Bragg's angle and

B=full width at half maximum

Morphological studies: The morphology and elemental composition of the as-synthesized composites were examined by a scanning electron microscope (SEM, JSM-7000F, JEOL) equipped with an Energy Dispersive X-ray Spectrometer (EDS). For the SEM experiment, the samples are coated with platinum to prevent any surface charging. The elemental composition of the nanocomposites synthesized at X=3.0 w/w% dopant fraction was analyzed by using EDS data.

Magnetic studies: The magnetic behaviour of the decomposed samples was studied on the commercial Vibrating Sample Magnetometer (VSM) Lakeshore (model73009). The magnetic hysteresis loops are measured at room temperature with a maximal applied magnetic field up to 0.95T. Magnetic field sweep rate is kept at 5Oe/s so that the measurement of the hysteresis loop with a maximum field of 0.989t is taken from with an interval of three hours. The saturation magnetization: coercivity and remanent magnetization are found from the hysteresis loop.

Result and Discussion

Structural and functional group studies

The Fourier Transform Infrared (FTIR) spectroscopy profiles for precursors and decomposed samples are presented in (Figure 1) while (Table 1): It is a summary of some important IR absorption bands of the as-prepared samples compared to metal oxalates in the literature [15,18,19]. The FT-IR spectra of the as-synthesized precursor composites and the corresponding decomposition products are presented in (Figure 2). The principal FTIR characteristic absorption bands of the samples (x=0.0, 0.1, 0.3, 3.0, and 5.0%) and their assignments are summarized in (Table 1). The profiles of all the samples in the series of precursors and decomposed products show peaks at similar wave number to those reported in the literature [15,18,19] for hydrated metal oxalate and the profiles were similar within each series but differed between the series, indicating the variation in bonding modes in the doped samples. However, within each series, slight insignificant but relevant shifts are revealed as the doping fractions increased. The shift is attributed to the presence of nickel ions in the microstructure of CoO/Co(OX), and the insignificance in variability between the profiles after doping can be attributed to the closeness of the bonding properties between nickel ions and cobalt ions [20]. In the decomposed products and for all doping fractions, two absorption bands are observed at 542cm^{-1} and 358cm^{-1} corresponding to

metal-oxygen bonds (Ni—O and Co—O, respectively), which is in agreement with the expected results. The absence of the free carbonyl [ν(C=O)] vibration expected at approximately 1700cm^{-1} is an indication that the carboxylate group is completely involved in the coordination.

Table 1: Some important IR absorption bands for the cobalt oxalate samples investigated in this work.

Cobalt Oxalate (0.0)	0.1	0.3	0.5	1	3	5	Literature Bands (cm^{-1})	Assignments (Stretching/Bending Vibrations)
3313	3340	3341	3348	3355	3382	3382	3200-3600	ν O-H
1532	1539	1553	1553	1553	1553	1553	1460, 1493 & 1535	ν_{as}COO-
1332	1336	1336	1336	1342	1342	1342		ν_{s}COO-
1236	1240	1278	1281	1281	1281	1281	1000-1300	ν C-O
1234	1236	1236	1236	1236	1236	1236	1000-1300	ν C-O
746	747	748	749	750	761	761	720-760	σOCO
659	652	652	653	657	657	657	550-650	ν_{as}Co-O
495	496	497	498	498	505	511	450-500	ν Ni-O/Co-O in CoO[21]

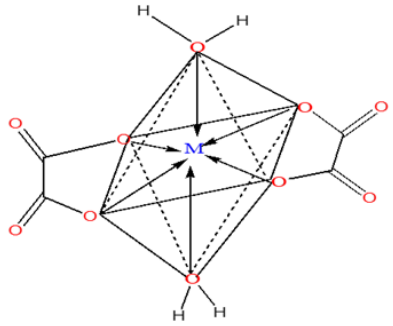

Figure 1: The three possible modes of the metal oxalate dihydrate.
Structure III: bridging bidente mode.

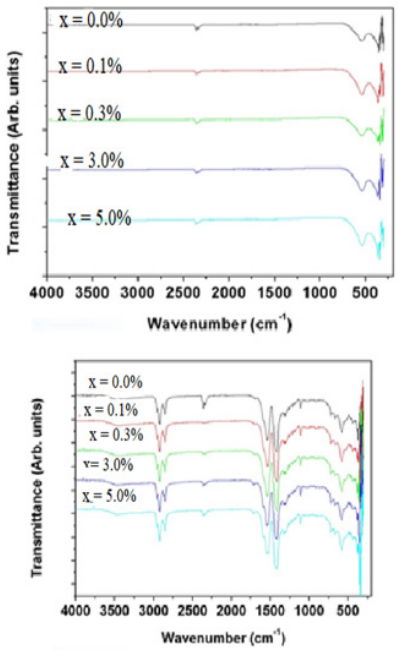

Figure 2: FT-IR profiles for (a)Ni-Co oxalate and (b) decomposed samples

However, there are variations in the exact peak position between 500 to 450 wave numbers, which may be attributed to the function of the metal present in the oxalate complex. The broad band at 3313cm^{-1} is attributed to the stretching vibration of O-H (metal hydroxyl and/or hydroxyl of water molecules of crystallization). The strong band at 1553cm^{-1} is attributed to the antisymmetric stretching vibration modes of the carbonyl group C=O of oxalates, while the bands at 1281cm^{-1} and 1236cm^{-1} are those of C-O symmetric stretching mode. The bands at 761cm^{-1} are attributed to the bending vibration of O-C-O, and the band at 629cm^{-1} to H-O-H rocking. Furthermore, the bands at 550-650cm^{-1} are attributed to the metal oxalate (Co-O) while the appearance of the bands around (495-510)cm^{-1} is attributed to the stretching vibration of the Co-O in CoO [21] and Ni-O bond [19].

These bands suggest the presence of the cobalt (II) ion with the band in the range 450-515cm^{-1} related to the Co-O vibrations in the octahedral site. The broad band at 3313cm^{-1} indicates the O-H stretch linked to the rapid energy relaxation caused by hydrogen bonding. This indicates the presence of exchangeable protons, typically of alcohol esters, and carboxylic acids. A shift to higher wave number is observed with doping and increase in the concentration of the dopant in the structure of the precursor. This observation can be attributed to the reduction in the mass of the samples and stronger bonds associated with nickel ions. Generally, more energy is required to stretch than to bend a bond, which explains why bands due to stretching occurs at higher wave numbers. The shifts in $n_{as}COO^{-}$ and $n_{s}COO^{-}$ are almost constant due to the similarity in the chemistry of nickel and cobalt and these are the bands directly linked to the metal atom. In addition, the difference in the peak intensities observed could be attributed to the different vibrations of the various functional group environments present in the molecule. The intensity of a peak depends on the magnitude of the dipole moment associated with the bond. Therefore, a bond with a strong dipole moment will have a stronger peak. The O-H bond has a strong dipole moment due to the difference in electronegativity between oxygen and hydrogen atoms. Furthermore, strong polar bonds such as carbonyl (C=O) will produce stronger peaks. The

Oxalate ligand has possibilities of three bonding modes in the Metal oxalate dihydrate complex as shown in (Figure 1): (Monodentate: Structure I), (Chelating bidentate: Structure II) and (Bridging bidentate: Structure III).

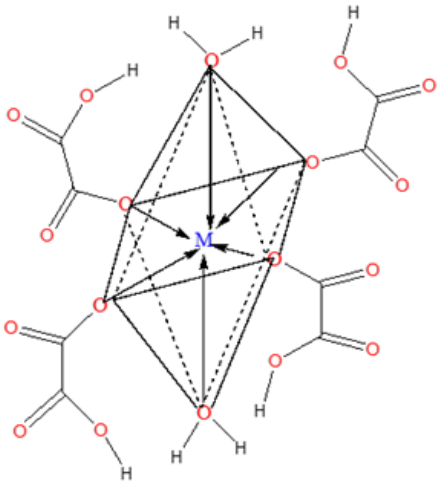

Structure I: Monodétente mode.

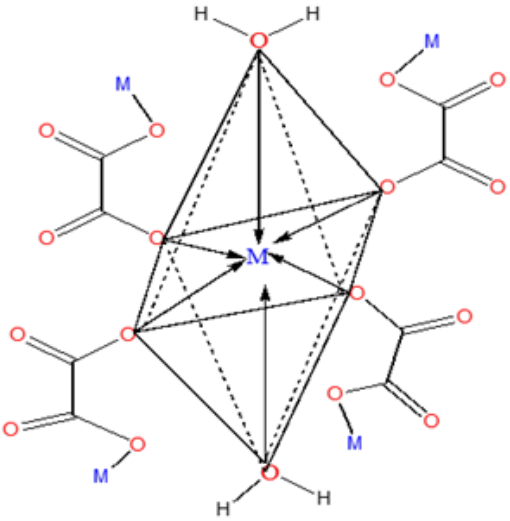

Structure II: Chélation bidente mode.

To elucidate the mode of coordination between the metal ions and the ligand in sample complexes, two different IR spectral schemes [20,21] were tested. According to the scheme by [21]; of the three principal modes possible (Figure 1), monodentate coordination (structure I) is favoured if the $n_{as}COO^-$ and n_sCOO^- are shifted to higher and lower frequencies, respectively (relative to the sodium salt), while for chelating bidentate coordination (structure II) and bridging bidentate (structure III), both the $n_{as}COO^-$ and n_sCOO^- frequencies will change in the same direction, since the bond orders of both CO bonds would change by the same amount. The shifts in $n_{as}COO^-$ and n_sCOO^- were calculated for the complexes (precursors). Waddington and co-workers [20], $Dv<100cm^{-1}$ suggests structure II while $Dv@150cm^{-1}$ and $Dv@164cm^{-1}$ imply, respectively, structures II, and III. In our samples, the Dv values lie above $200cm^{-1}$ and are assigned structure III (bridging bidentate), especially since the oxalate functions participate in the bonding which resulted in the formation of a polymeric structure generally called metal organic framework, (Figure 3).

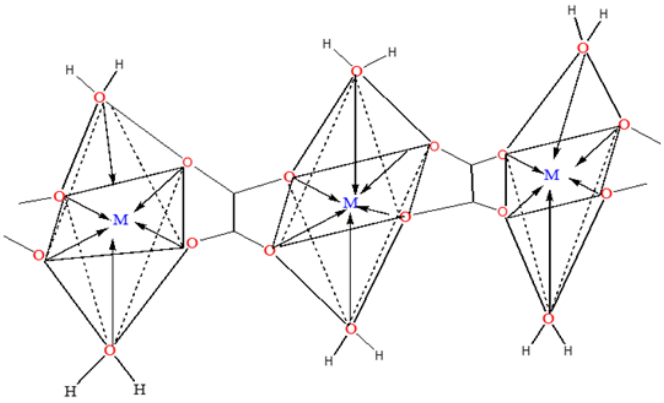

Figure 3: Prospective metal organic framework.

Thermo Gravimetric Analysis (TGA)

The TGA analysis shows the decomposition profile of the precursor and suggests the decomposition temperature of the samples. (Figure 4) shows the TGA/DTG profiles of two precursors (x=0.0w/w% and 3.0w/w%) and the species present at various decomposition stages. The TGA results show two principal weight loss regions: the first with a percentage weight loss of 19.34% observed compared with 19.62% calculated and corresponding to the loss of water of crystallization. The second weight loss portion of 39.7% compared with (39.34, 34.72, and 36.38) % is attributed to the decomposition of the anhydrous metal oxalate to the metal oxide while evaporating carbon dioxide and/or carbon monoxide (Figure 5).

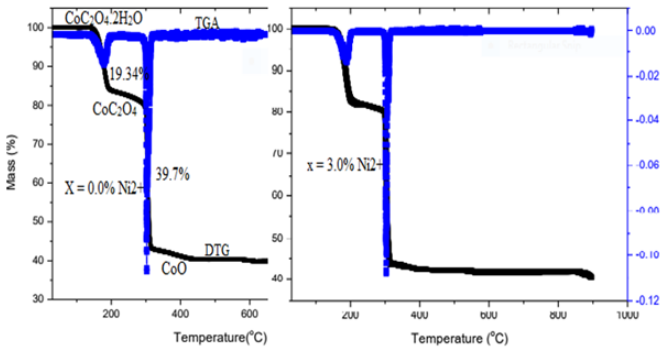

Figure 4: TGA/DTG results of the precursor: $CoC_2O_4.2H_2O$.

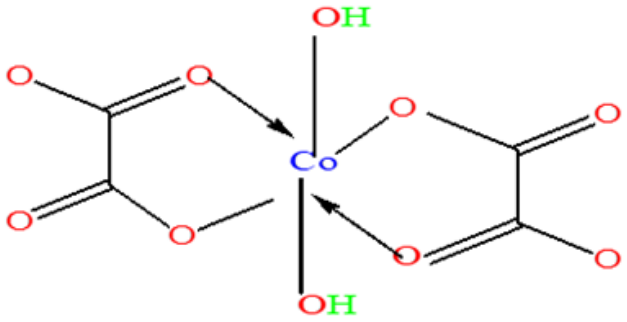

Figure 5: Possible decomposition profiles.

$$CoC_2O_4.2H_2O \rightarrow CoC_2O_4 \rightarrow CoO_{(s)}$$

One mole of Cobalt oxalate dihydrate decomposed at 180-200 °C to COC_2O_4 losing $2H_2O$ of crystallization (19.34/19.62%) and the later decomposed at 200-300 °C to CoO (39.7/39.34%) giving off $CO(g)+CO_2(g)$.

$$2CoC_2O_4.2H_2O \rightarrow 2CoC_2O_4 \rightarrow Co_2O_{3(s)}$$

Two moles of Cobalt oxalate dihydrate decomposed at 180-200 °C to $2CoC_2O_4$ losing $4H_2O$ of crystallization (19.34/19.62%) and the later decomposed at 200-300 °C to CO_2O_3 (39.7/34.72%) giving off $3CO(g)+CO_2(g)$.

$$3CoC_2O_4.2H_2O \rightarrow 3CoC_2O_4 \rightarrow Co_3O_{4(s)}$$

Three moles of Cobalt oxalate dihydrate decomposed at 180-200 °C to $3CoC_2O_4$ losing $6H_2O$ of crystallization (19.34/19.62%) and the later decomposed at 200-300 °C to Co_3O_4 (39.7/36.38%) giving off $4CO(g)+2CO_2(g)$.

The observed decomposition profile suggests that the precursor molecules are in the form of a polymer and do not occur in isolation, but rather, the metal oxalate framework or polymeric network which decomposes at 300 °C to different phases of the metal oxide (CoO, Co_2O_3, and Co_3O_4). However, the calculations of the decomposition residue (41.04% for CoO, compared more with 40.96 theoretical) in conformity with the suggestion that CoO is the principal decomposition product but with a possible presence of the oxalate fraction in the microstructure of the decomposed products. Interestingly, the decomposition temperature observed in the present study (300 °C) is lower than 450 °C reported by Nguimezong et al. [18] although with a similar profile. The change in decomposition temperature indicates a change in either phase, stoichiometry or particle properties.

Phase analysis of calcined powder (Powder X-ray diffraction (PXRD))

The decomposition products obtained by pyrolysis of the precursors at 350 °C for 3 hours in air were analysed by X-Ray Powder Diffraction (PXRD). The XRD patterns for the doped samples are shown in (Figure 6a), while that of the decomposition product for pure nickel sample are shown in (Figure 6b). The patterns for the decomposition products were indexed with ICDD files for Cobalt, CoO, Co_3O_4, and Nickel Oxide (as- synthesized). The XRD pattern obtained for the decomposition product summarized in (Table 2), which revealed crystallinity with major peaks at 2θ values 23.12, 36.60, 42.44, 66.30, 73.82 and 77.65 corresponding to (111), (200). (220), (311). And (222) lattice planes, respectively, of Face Centred (FCC) Cobalt (II) Oxide which matched with the XRD pattern of CoO JCPDS card number 78-0431 and two weak peaks observed at 2θ values 21.19 and 52.68, Matched with carboxylate peaks in the precursor (Figure 6b). No other obvious peaks of impurities were seen in this pattern for x=5.0% Ni^{2+} concentration. The absence of the Ni peaks in the profile indicated that nickel ions failed to modify the microstructure of the composite for x≤5.0%. However, the shift in 2ϖ values observed for the doped samples is indicative of the presence of a dopant associated with the difference in ionic radus between Ni^{2+} (0.078nm) and Co^{2+} (0.072). These results confirm that the samples synthesized were Nanocomposites Cobalt oxide impregnated with Oxalate Co(ox) and doped with Ni^2. The crystallite sizes were found to vary between 20.22nm and 33.13nm for various identified diffraction peaks.

Table 2: Powder X-ray diffraction peaks for the decomposed samples indexed with ICDD (JCPDS card number 78-0431) exhibiting CoO.

2Θ						hkl	Intensities
Peak No	X=0.0 %	X=0.5 %	X=3.0 %	X=5.0 %	X=40.0%		
1	22.29	22.29	22.29	22.29	22.29	# (OX)	24.4
2	36.66	36.60	36.58	36.57	36.55	(111)	35.9
3	42.45	42.44	42.43	42.42	42.42	(200)	100
4	52.70	52.68	52.68	52.68	52.68	# (OX)	36.6
5	67.90	67.86	67.81	67.8	67.79	(220)	10.1
6	72.81	72.76	72.75	72.74	72.24	(311)	20.3
7	77.67	77.66	77.65	77.63	77.64	(222)	32.6
D(nm)	20.22	30.53	33.13	26.84	23.95		

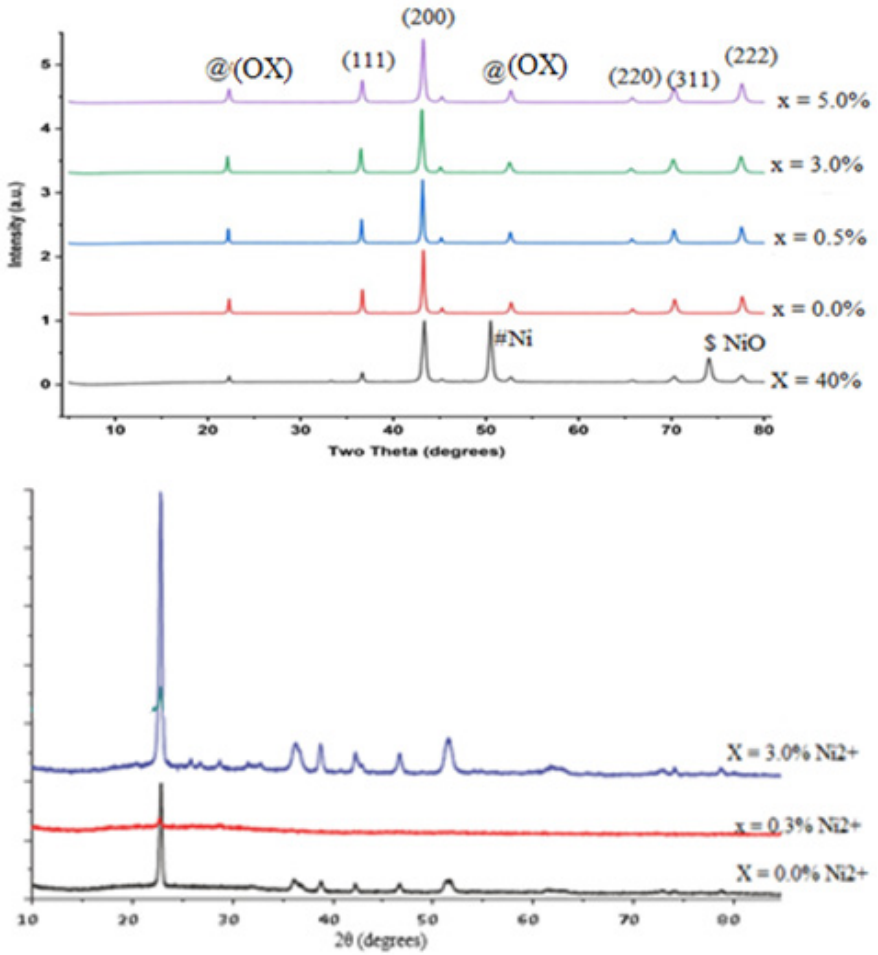

Figure 6: XRD for (a) decomposition products (b) precursors (metal oxalates).

Morphology and elemental composition studies

Morphology and composition analyses of the nanocomposite (Figure 7) shows the SEM images of as-synthesized and Nickel doped Nanocomposite, which were fabricated at different Nickel ions (dopant concentrations; x=x=0.0, 0,1, 0.3, 3.0 and 5.0%) compositions and heat-treated temperatures of 350 °C. The SEM images reveal a change in the morphology of the Nano particles with doping which modifies with increase in the concentration of the dopant (x=0.0, 0,1, 0.3, 3.0 and 5.0%). The first image, (Figure 7a) (x=0.0%) shows Nano-particles with cubic morphology for pure cobalt oxide while (Figure 7b) (x=0.1%) reveals distorted cubic morphology. As the concentration of the dopant (Ni^{2+}) further increased (to x=3.0 %), (Figure 7c), an entirely new morphology is observed (Nano tubes). The change is attributed to the presence of Nickel ions in the cobalt oxide/Co (OX) microstructure which is linked to the difference in ionic radius between Ni^{2+} (0.078nm) and Co^{2+} (0.072). Ni^{2+} has a greater ionic radius and upon substitution in the Co^{2+} sites, it introduces an accommodation space problem. To overcome this problem, restructuring of the particle's coordination number occurs (the lattice parameter a, increases as the larger Ni^{2+} ions replace the smaller Co^{2+} ions) leading to a change in the structure from a normal cube to a distorted cubic. As a consequence, the number of voids has increased leading to the change in morphology. As the concentration of the dopant increased to x=3.0%, the distorted cubic structures interconnect into nano-tubes. These Nanotubes give high surface to volume ratio and short path lengths for cation transport, giving rise to fast charging capabilities and the materials can be exploited in recharge systems. However, with a further increase in the dopant concentration to x=5.0 %, (Figure 7d), the interconnected nanotubular network collapses back into cubic micro agglomerates. This observation is consistent with the study on critical doping w/w% effects [22].

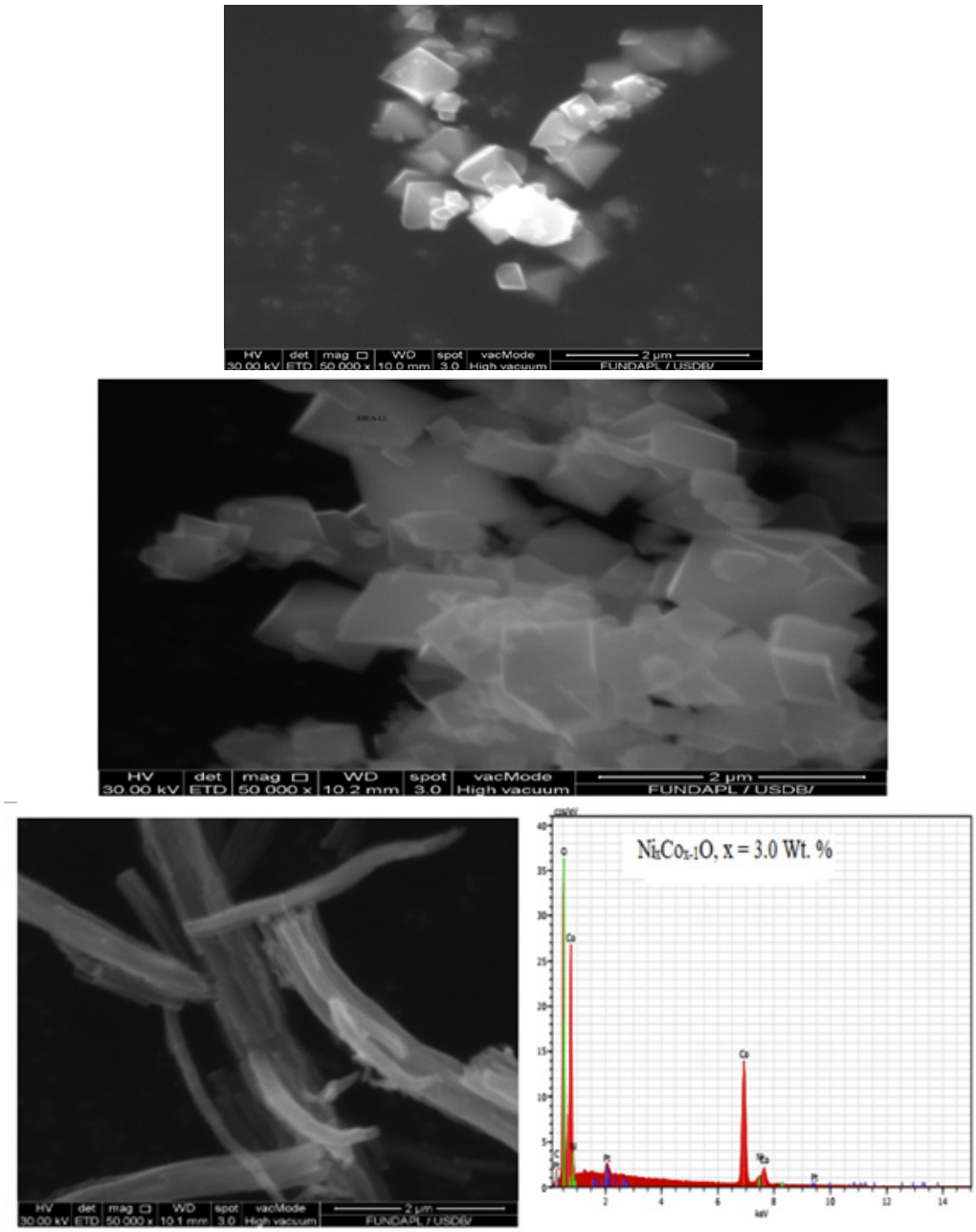

Figure 7: a) SEM image of pure $Ni_xCo_{x-1}O/Co(OX)$ (x=0),
b) SEM image of $Ni_xCo_{x-1}O/Co(OX)$ (x=0.5),
c) SEM/EDS Image of $Ni_xCo_{x-1}O/Co$ (OX) (x=3.0),
d) SEM Image of $Ni_xCo_{x-1}O/Co$ (OX) (x=5.0)

The average diameters of the nanocomposites in the various morphologies are measured to be in the range of 20-50nm, although they increase slightly with increasing dopant concentration. These results show great correlation with the nanocrystal size values calculated using Scherrer formula from XRD data, which is evident that the product consists of homogeneous nanocrystals with little or no agglomeration. EDS mapping images of the sample with dopant concentration (x=0.3%) were obtained, as can be seen in Fig. 6c and the elemental mapping images support the fact that both Ni^{2+} ions and Co^{2+} ions coexist in the nanocomposite examined nanotubes. Furthermore, only cobalt, nickel and oxygen are present in the matrix, which confirmed the purity of the as-prepared sample. Therefore, EDS mapping images confirm that the changes observed in the microstructure as revealed from XRD and the morphology from SEM to be as a result of the replacement of Co^{2+} ions with Ni^{2+} ions in the microstructure of the composites.

Magnetic studies

(Table 3) shows a summary of the magnetic properties while (Figure 8) shows the room-temperature hysteresis loop which shows

No appreciable hysteresis, negligible width of the loop, negligible remnant magnetizations, and no saturated magnetizations suggesting Supper Paramagnetic behaviour of the synthesized Ni-CoO nanoparticles. Accordingly, the magnetization at saturation (M_s) are estimated to be only 0.045emu/cm^3, 0.015emu/cm^3, and ≤0.010emu/cm^3 for Ni ions dopant concentrations of (3.0%, 0.1% and 0.0, 0.5, 5.0 and 40.0%) respectively (The saturation magnetization Ms were determined from the extrapolation of curve of H/M versus H) [23]. Cobalt oxide nanoparticles are made of small single domains, each characterized by its own magnetic moment oriented randomly, and the total magnetic moment of the nanoparticles is the sum of these magnetic domains coupled by dipolar interactions resulting in low values of Mr. The variation in magnetic properties of nanomaterials with doping and dopant concentration is attributed to changes in morphology, sample size and sample shape. The absence of saturation in fields stronger than the coercivity suggests that the synthesized Ni-CoO samples contain a certain amount of superparamagnetic Ni nanoparticles (d<20nm) [24]. These particles and disordered spins at the Ni-CoO interface contribute to the strong-field portion of the hysteresis loop of the Ni-CoO. The relatively small Mr/Ms ratio (Mr/Ms<0.5), between the remanent magnetization Mr and the saturation magnetization M_s (Figure 8), shows that the nano composites are soft magnetic materials. These "soft materials" show low residual magnetism (M_r) (Figure 8), one main physical property of NPs used in negative contrast enhancing agents for Magnetic Resonance Imaging (MRI) [25,26]. Furthermore, the presence of oxalate can serve as a coating on the surface of the Ni-CoO. One of such, carbohydrate-coated iron-based nanoprobe, has already been approved by FDA for clinical use [27]. The presence of this coat or functional (bio)molecules at their surface may prevent dissolution, early phagocytosis, and toxicity by improving the emitted signal or target-specific sites such as tissues, cells, enzymatic activity, or genome [28]. In this regards, our synthesized samples may offer great flexibility of applications in a variety of experimental settings. The residual magnetization and coercivity obtained in this study are in the same range as those reported for $Zn_{0.5}Co_{0.5}Fe_2O_4$ [29]. As observed from (Figure 8), at the critical dopant fraction (x=3.0w/w% Ni) the soft super magnetic material passes to a hard super magnetic phase suggesting that depending on the dopant concentration the synthesized nanocomposites are multifunctional.

Table 3: Summary of magnetic properties of the synthesized samples.

Sample	X=0.0%	X=0.1%	X=0.5%	X=3.0%	X=5.0%	X=40.0%
Saturation magnetization maxim measured M_s emu	1.48×10^{-02}	1.49×10^{-02}	8.97×10^{-03}	4.52×10^{-02}	7.0×10^{03}	7.75×10^{-03}
H_c O_c Coercive field, field at which M//H changes sign	48.013	20.314	17.675	108.271	15.539	26.859
Mr enu remenant magnetic M at H=0	2.79×10^{-04}	1.20×10^{-04}	8.72×10^{-05}	2.44×10^{-03}	1.30×10^{-04}	1.77×10^{-04}
H_s (Oe) saturation field, field at which M reaches 0.95Ms	5715.93	5716.14	5679.01	5610.88	5780.16	5559.87
Maximum H measured Hmax O_c	5997.5	5997.5	5997.5	5997.5	5998	5997.5
Area O_e*	2.08	7.51×10^{-01}	5.02×10^{-01}	$2.14\times10^{+04}$	9.46×10^{-01}	5.67×10^{-01}
Maximum permeability	5.55×10^{-05}	5.52×10^{-06}	4.52×10^{06}	2.19×10^{-05}	7.44×10^{-06}	6.17×10^{-06}
M_r/M_s	0.0188	0.0081	0.0097	0.0540	0.01857	0.0228

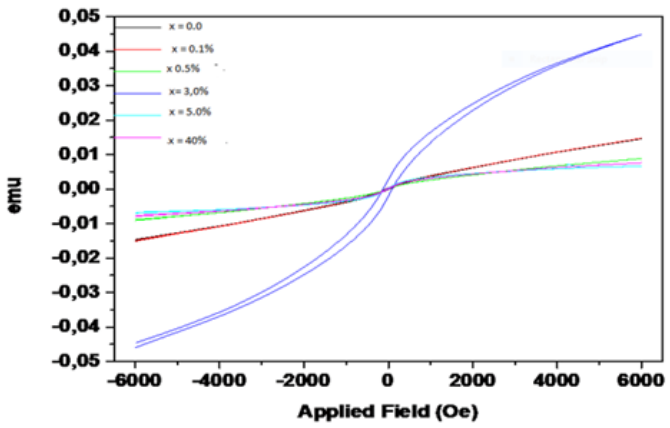

Figure 8: Room-temperature hysteresis loop of the as-synthesized Ni-CoO nanoparticles.

The profile for the Correlation between dopant concentration (x/%), Particle size (D/nm), and magnetic properties is shown in (Figure 9). The crystallite sizes increased with an increase in dopant concentration to a critical size of 33.13nm at 3.0 w/w% Ni doping and then decreased as the nanotubular morphology reconstituted into distorted cubic nanocomposites. This result suggested that the replacement of Ni^{2+} atoms for Co^{2+} in the host microstructure is prevalent for concentrations up to 3.0w/w%, after which it gave way to the adsorption of Ni atoms in the pores. Thus, suggesting modification of the morphology and eventual breakdown at very high doping fractions. These results are in conformity with XRD results which indicated the presence of both Ni^{2+} and NiO peaks in the microstructure of the sample with dopant concentration X=40.0w/w%. This correlation reflects strongly between the particle size, morphology, and magnetic properties while respecting the critical dopant fraction of 3.0 w/w% for particle size and magnetic properties.

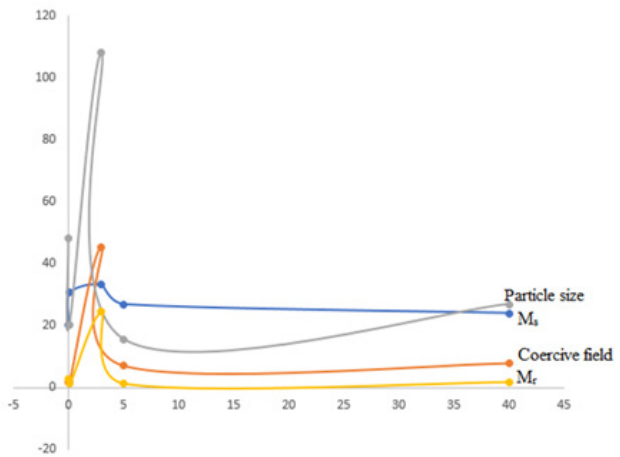

Figure 9: Correlation profile between dopant concentration (x), Particle size, and magnetic properties.

Conclusion

The results obtained in the present study indicate that Magnetic $Ni_xCo_{1-x}O/Co_3O_4$ Nanoparticles composites with potential applications in negative contrast enhancing agents for Magnetic Resonance Imaging (MRI have been synthesized by modified oxalate rout using carambola fruit juice. The particles produced were nano-sized, pure, Stoichiometric, and discrete (crystalline). Finally, both the presence of a dopant and the dopant concentration have revealed modifying effects on the particle size, morphology, and magnetic properties of the nano-structured material synthesized without altering the microstructure of the host oxide. We can conclude by saying that in this project, nanosized particles of magnetic cobalt oxide and nickel doped cobalt heterometallic oxide systems have been successfully synthesized while eliminating the problems often associated with other synthesis techniques such as high calcination temperature, laborious powder preparation stages, deviations from stoichiometric ratio of cations, use of solvents which are environmentally unfriendly and the usual solubility problem often encountered using commercial oxalic acid as a precipitating agent.

Data Availability

The datasets generated during and/or analyzed during the current study that are not included in this article are available from the corresponding author upon reasonable request.

Ethical Approval

This article does not contain any studies with human participants or animals performed.

References

1. Zhang Y, Fei C, Liu Y, Wang R, Yan G, et al. (2010) The effect of surface modification on the magnetic properties of $CoFe_2O_4$ nano-particles synthesized by the hydrothermal method. J Nanosci Nanotechnol 10: 6395-6399.
2. Stankic S, Suman S, Haque F, Vidic J (2016) Pure and multi metal oxide nanoparticles: synthesis, antibacterial and cyto- toxic properties. Journal of Nanobiotechnology 14(1): 73.
3. Gubin SP, Koksharov YA, Khomutov GB, Yurkov GY (2005) Magnetic nanoparticles: Preparation, structure and properties. Russ Chem Rev 74(6): 489-520.
4. Petrarca C, Poma AM, Vecchiotti G, Bernardini G, Niu Q, et al. (2020) Cobalt magnetic nanoparticles as theranostics: Conceivable or forgettable? Nanotechnology Reviews 9(1): 1522-1538.
5. Faraji M, Yamini Y, Rezaee M (2010) Magnetic nanoparticles: Synthesis, stabilization, functionalization, characterization, and applications. J Iran Chem Soc 7: 1-37.
6. Wu W, Wu Z, Yu T, Jiang C, Kim WS (2015) Recent progress on magnetic iron oxide nanoparticles: Synthesis, surface functional

strategies and biomedical applications. Sci Technol Adv Mater 16(2): 023501.

7. Choi CJ, Dong XL, Kim BK (2001) Microstructure and magnetic properties of Fe nanoparticles synthesized by chemical vapor condensation. Mater Trans 42: 2046-2049.
8. Li J, Shi X, Shen M (2014) Hydrothermal synthesis and functionalization of iron oxide nanoparticles for MR imaging applications. Part Part Syst Charact 31(12): 1223-1237.
9. Foroughi F, Hassanzadeh-Tabrizi SA, Bigham A (2016) In situ microemulsion synthesis of hydroxyapatite-$MgFe_2O_4$ nanocomposites as a magnetic drug delivery system. Mater Sci Eng C 68: 774-779.
10. Wang WW (2008) Microwave-induced polyol-process synthesis of MII Fe2O4 (M=Mn, Co) nanoparticles and magnetic property. Mater Chem Phys 108: 227-231.
11. Cabrera L, Gutierrez S, Menendez N, Morales MP, Herrasti P (2008) Magnetite nanoparticles: Electrochemical synthesis and characterization. Electrochim Acta 53(8): 3436-3441.
12. Saif M, Aboul-Fotouh S, El-Molla S, Ibrahim M, Ismail L (2012) Improvement of the structural, morphology, and optical properties of TiO_2 for solar treatment of industrial wastewater. Nanotechnology for Sustainable Development pp. 101-111.
13. Makhlouf MT, Abu-Zied BM, Mansoure TH (2013) Effect of calcination temperature on the H_2O_2 decomposition activity of nano-crystalline Co_3O_4 prepared by combustion method. Applied Surface Science 274: 45-52.
14. Sun H, Liang h, Zhou G, Wang S (2013) Supported cobalt catalysts by one-pot aqueous combustion synthesis for catalytic phenol degradation. Journal of Colloid and Interface Science 394: 394-400.
15. Bashar Issa, Obaidat IM, Albiss BA, Haik Y (2013) Magnetic nanoparticles: surface effects and properties related to biomedicine applications. Int J Mol Sci 14(11): 21266-21305.
16. Raveau B, Seikh M (2012) Cobalt oxides: From crystal chemistry to physics. First Edition. Wiley-VCH Verlag GmbH & Co. KGaA, US.
17. Ghosh M, Sampathkumaran EV, Rao CNR (2005) Synthesis and magnetic properties of CoO nanoparticles. Chem Mater 17(9): 2348-2352.
18. Nguimezong MBN, Foba-Tendo J, Yufanyi DM, Etape EP, Eko JN, et al. (2014) Averrhoa carambola: A renewable source of oxalic acid for the facile and green synthesis of divalent metal (Fe, Co, Ni, Zn, and Cu) oxalates and oxide nanoparticles. Journal of Applied Chemistry.
19. Li Y, Qiu W, Qin F, Fang H, Hadjiev VG, et al. (2016) Identification of cobalt oxides with Raman scattering and fourier transform infrared spectroscopy. The Journal of Physical Chemistry C 120(8): 4511-4516.
20. Alcock NW, Tracy VM, Waddington TC (1976) Acetates and acetato-complexes. Part 2. Spectroscopic studies. J Chem Soc Dalton Trans pp. 2243-2246.
21. Mesubi MA (1982) An infrared study of zinc, cadmium and lead salts of fatty acids. Journal of Molecular Structure 81(1-2): 61-71.

22. Lambi JN, Takop AN, Nkongho E, Lazaro FRC, Alejandro JA (2003) Synthesis, spectral properties and thermal behavior of zinc acetylsalicylate. Thermochemica Acta 398(1-2): 145-151.

23. Nethravathi C, Sen S, Ravishankar N, Rajamathi M, Pietzonka C, et al. (2005) Ferrimagnetic nanogranular Co_3O_4 through solvothermal decomposition of colloidally dispersed monolayers of α-cobalt hydroxide. Phys Chem B 109(23): 11468-11472.

24. Gusev AI, Rempel A (2004) Nanocrystalline materials. Cambridge: Cambridge International Science, USA, p. 351.

25. Zheng J, Ren W, Chen T, Jin Y, Li A, et al. (2017) Recent advances in superparamagnetic iron oxide based nanoprobes as multifunctional theranostic agents for breast cancer imaging and therapy. Curr Med Chem 25(25): 3001-3016.

26. Arias LS, Pessan JP, Vieira APM, de Lima TMT, Delbem ACB, et al. (2018) Iron oxide nanoparticles for biomedical applications: A perspective on synthesis, drugs, antimicrobial activity, and toxicity. Antibiotics (Basel, Switzerland) 7(2): 46.

27. Shah A, Mankus CI, Vermilya AM, Soheilian F, Clogston JD, et al. (2018) Feraheme® suppresses immune function of human T lymphocytes through mitochondrial damage and mitoROS production. Toxicol Appl Pharmacol 350: 52-63.

28. Wu K, Su D, Liu J, Saha R, Wang JP (2019) Magnetic nanoparticles in nanomedicine: A review of recent advances. Nanotechnology 30(50): 502003.

29. Sattarahmady N, Zare T, Mehdizadeh AR, Azarpira N, Heidari M, et al. (2015) Dextrin-coated zinc substituted cobalt-ferrite nanoparticles as an MRI contrast agent: in vitro and in vivo imaging studies. Colloids Surf B Biointerf 129: 15-20.